ONCOIMMUNOLOGY
2026, VOL. 15, NO. 1, 2660418
https://doi.org/10.1080/2162402X.2026.2660418

Taylor & Francis
by informa

RESEARCH ARTICLE

Spatial transcriptomics unveils immune cellular ecosystems associated with patient survival in diffuse large B-cell lymphoma

Alba Diaz-Herrero[a], Héctor Fernando Pelaez-Prestel[b], Lucile Massenet-Regad[a,c], Maëva Veyssiere[a], Julien Calvani[a,d], Caterina Cristinelli[e,f,g], Jacqueline Lehmann-Che[a], Véronique Meignin[d], Catherine Thieblemont[e,f,g], Véronique Blanc[h], Vassili Soumelis[a,i] and Pierre Tonnerre[a]

[a]Institut de Recherche Saint-Louis, Université Paris-Cité, Inserm U1342, Paris, France; [b]School of Medicine, Department of Immunology, Complutense University of Madrid, Madrid, Spain; [c]Mnemo Therapeutics, Paris, France; [d]Pathology Department, hôpital Saint-Louis, AP-HP, Paris, France; [e]Université Paris Cité, Paris, France; [f]Assistance Publique – Hôpitaux de Paris, Hôpital Saint-Louis, Hemato-oncologie, Paris, France; [g]Inserm U1153, Hôpital Saint-Louis, Paris, France; [h]Institut de Recherches Servier, Gif-sur-Yvette, France; [i]Department of Immunology-Histocompatibility, Saint-Louis Hospital, AP-HP Nord, Université Paris Cité, Paris, France

ABSTRACT

Diffuse large B-cell Lymphoma (DLBCL) is the most prevalent subtype of non-Hodgkin's lymphoma for which current therapeutic strategies remain insufficient, in part owing to heterogeneity in tumor biology and the immune microenvironment. The diffuse nature of DLBCL represents a challenge to elucidate how malignant and immune cells are spatially organized within the tumor microenvironment (TME), and how this organization impacts immune function and clinical outcome. Here, we performed a pilot spatial transcriptomics analysis of primary DLBCL tissue sections to resolve spatial gene expression patterns and cell–cell interactions, with key cellular features validated at the protein level. We identified six recurrent, spatially organized cellular ecosystems (Cell-Eco) defined by distinct immune compositions, transcriptional programs, and neighborhood architectures. Notably, ecosystems with similar immune cell abundance exhibited divergent functional states and opposite clinical associations, demonstrating that spatial context and local interactions, rather than cell-type frequency alone, shape immune function within the DLBCL TME. Building on these spatial ecosystems, we derived Cell-Eco gene signatures that generated prognostic scores and robustly stratified patient survival in large, independent DLBCL cohorts comprising more than 1000 cases. Across ecosystems, tumor-associated macrophages have emerged as the dominant spatial partners of malignant B cells, highlighting their central role in structuring the immune microenvironment. Together, these findings establish a spatially informed framework for DLBCL immune organization and demonstrate the prognostic relevance of tumor cellular architecture.

ARTICLE HISTORY

Received 17 January 2026
Revised 06 April 2026
Accepted 11 April 2026

KEYWORDS

Diffuse large B-cell lymphoma (DLBCL); spatial transcriptomics; cellular ecosystems; tumor microenvironment (TME); tumor-associated macrophages

CONTACT Pierre Tonnerre pierre.tonnerre@inserm.fr Institut de Recherche Saint-Louis, Université Paris-Cité, Inserm U1342, F-75010, Paris, France

Supplemental data for this article can be accessed online at https://doi.org/10.1080/2162402X.2026.2660418.

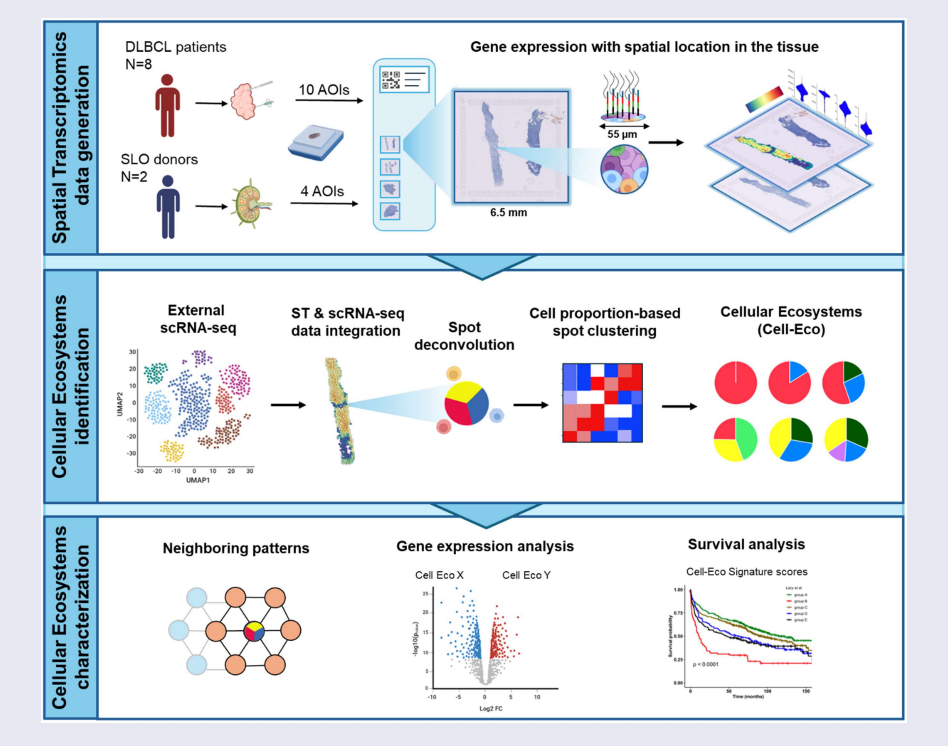

Introduction

Diffuse large B-cell lymphoma (DLBCL) is the most common subtype of non-Hodgkin's Lymphoma (NHL) worldwide and accounts for approximately 40% of all cases.[1] Despite the significant improvements in patient outcomes with first-line treatment with R-CHOP (rituximab, cyclophosphamide, doxorubicin, prednisone, and vincristine), approximately 40% of the patients experience relapse or become refractory.[2] A deeper understanding of the biological mechanisms driving disease progression is essential for developing new therapies with increased response rates and improved overall survival.

The study of the tumor microenvironment (TME) has become of great importance in elucidating the factors that contribute to disease progression and relapse in DLBCL. Both the cellular composition and spatial organization have been linked to disease stage and response to treatment in various solid cancers.[2-4] However, a hallmark of DLCBL is its diffuse pattern, characterized by the scattered distribution of malignant cells within the TME,[1,4] hindering a comprehensive assessment of the spatial architecture and associated cell states in DLBCL. Previous studies investigating the cellular composition and gene expression profiles in the TME of DLBCL have provided important insights into the heterogeneity of immune cell infiltration and its connection to tumor progression,[5] treatment resistance, and clinical outcomes.[5-8] Nevertheless, these characterizations were limited by the lack of spatial context of the immune cell profiles, including their localization within the TME and the associated communication pathways. Recent studies have integrated tissue coordinates into a detailed analysis of the DLBCL TME, using high parameter imaging[9-12] or digital spatial profiling of macrophages.[13] However, these studies faced technical constraints such as the limited number of parameters analyzed and a narrow focus on specific immune cell types. A comprehensive characterization of the different cellular immune profiles within the tissue topology, integrating spatial localization, cellular interactions, and communication patterns, is still missing in DLBCL.

In this study, we applied spatial transcriptomics to generate a high-resolution map of gene expression within the tissue architecture of ten primary DLBCL samples as a discovery cohort. A preprint version of this work was previously made available.[14] We demonstrate that DLBCL tissues are organized into discrete cellular ecosystems (Cell-Eco) characterized by distinct immune cell compositions, transcriptional programs, and intercellular communication networks. Leveraging these spatial ecosystems, we derived ecosystem-associated transcriptomic signatures that capture functional immune states and are associated with overall

survival in independent patient cohorts. As a pilot spatial analysis, this work highlights the value of resolving the spatial organization of the DLBCL tumor microenvironment to uncover biologically meaningful patterns with prognostic relevance and to inform future biomarker development and therapeutic strategies.

Materials and methods

Human sample collection and processing

Samples from DLBCL adult patients were obtained from the Pathology Department at the Hospital Saint Louis (Paris, France). The clinical characteristics of the patient samples are provided in Table S1. Non-metastatic reactive lymph node samples (rLN) and tonsils were obtained from surgical procedures at the Hospital Bichat and Robert Debré (Paris, France). Formalin-fixed paraffin-embedded (FFPE) samples were selected based on their RNA with a cutoff of DV200 ≥ 30%. The study was conducted over a four-year period, with sample collection beginning on July 16th, 2020.

Informed consent statement

This study involving human participants was reviewed and approved by the Comité Local d'Ethique pour la Recherche Clinique des HUPSSD Avicenne Jean Verdier-René Muret (Approval No. CLEA-2020-113). Written informed consent was obtained from all participants prior to sample collection. All samples were obtained following the principles of Good Clinical Practice and the Declaration of Helsinki.

Spatial transcriptome sequencing and preprocessing

Spatial transcriptomic (ST) data were generated from 10 DLBCL and 4 SLO (reactive lymph node and tonsil) samples across two experiments: 2 DLBCL and 2 SLO samples using Visium FFPE "Direct placement," and 8 DLBCL and 2 SLO samples using the "CytAssist-enabled" assay. From each block, 4 µm sections were placed on the slide capture areas, H&E-stained, deparaffinized, imaged, decrosslinked, and processed for probe hybridization, ligation, tissue removal, and library preparation per the User Guides. Libraries were sequenced on a NovaSeq6000 Sequencing System (Illumina, CA, USA), and FASTQ files were processed with the GRCh38 transcriptome using Space Ranger v2.0.1. Each sample was preprocessed individually on R (v4.3.2) with the package Seurat (v4.1.1) to retain spots expressing more than 500 genes and less than 10% mitochondrial genes. Data were normalized and scaled with *SCTransform*, and PCA on the 5000 most variable genes (variance-stabilizing transformation) was used for dimensionality reduction.

Single-cell RNA sequencing and spatial transcriptomic data integration

Public scRNA-seq data were preprocessed with Seurat (v4.1.1), retaining cells with ≥200 genes and <10% mitochondrial reads. Data were normalized, log2-transformed, and dimensionality reduced via PCA. Samples were integrated using Harmony, clustered, and annotated. Malignant B cells were identified with CopyKAT,[15] and clusters were annotated based on established marker genes. Malignant annotation was validated with copy number variation scores from inferCNV package (v.1.3.3; https://github.com/broadinstitute/inferCNV).

Following the pre-processing of ST data, genes were filtered to retain common genes between assays (Figure S5F). The spots of each sample were decomposed using the corresponding public scRNA-seq dataset (either DLBCL or SLO) as a reference. The cell type proportions per spot were generated using the probabilistic method RCTD[16] (Robust Cell Type Decomposition) on *multi-mode*. All genes selected from the scRNA-seq data for cell-type decomposition were included for all samples (Figure S5G).

Cellular ecosystems identification based on cell type composition

A matrix of cell-type proportions was constructed by merging the RCTD outputs of each DLBCL ST sample. Proportions lower than 10% were filtered out, and the remainder was rescaled to 100%. Leiden algorithm[17] (Python v3.x) with a cluster granularity of 0.2, was applied to identify groups of spots based on

similar cell composition. Spots were labeled as Cellular ecosystems (Cell-Eco) with cell-type means higher than 10% considered biologically significant. Spots were filtered and rescaled based on cell-type means per Cell-Eco. Differential expression analysis (DEA) based on the non-parametric Wilcoxon rank-sum test was performed between the Cell-Eco labels. Pathway enrichment analysis was performed on DEG using Metascape[18] and DisGeNET.[19]

Neighbor scores

Considering a maximum of six neighbors per spot, we applied the function *RegionNeighbors* of the package Semla to extract the cellular ecosystem's identity of spots spatially co-localizing. The neighbor score (*N* score) was calculated as the frequency of neighbor interactions by the following formula:

$$N\ score^{i}_{j\to k} = \frac{N^{i}_{j\to k}}{N_i}$$

where *j* is a Cell-Eco identity spatially located next to another unique identity, *k,* in sample *i*. Therefore, $N_{j\to k}$ refers to the number of Cell-Eco *j* neighbor to a Cell-Eco *k* in a sample *i*, divided by the total neighbors of the sample (N_i). The neighbor score of each group of samples was calculated as a mean of neighbor scores as follows:

$$N\ score^{g}_{j\to k} = \frac{\sum_{i}^{S_g} \frac{N^{i}_{j\to k}}{N_i}}{S_g}$$

where *g* is the identity of the group of samples, and *S* is the number of samples. Consequently, the neighbor score of a Cell-Eco *j* next to a Cell-Eco *k* per group *g* is the sum of neighbor scores of each sample *i* belonging to the group *g* divided by the total number of samples in the group S_g.

Spatial autocorrelation

Spatially autocorrelated genes were identified using the CorSpatialFeatures function of the Semla package based on Moran's I statistics.[20] Only spatial correlation scores greater than 0.5 were considered for gene selection.

Survival analysis

The signature for each Cell-Eco was defined as the fifth percentile of differentially expressed genes ($p < 0.05$ and |log2FC|>0.25) ordered by adjusted *p*-value. Signature scores for each cellular ecosystem were calculated as previously described by Liu et al.[13], scaled and centered prior to the hierarchical clustering for patient stratification. For the individual Cell-Eco signatures survival assessment, patients were divided into three groups based on their signature scores, with tertiles used as the cutoffs. The Cox proportional hazard model was compared to the tertile 1 group with the tertile 3 group to estimate the hazard ratio for each Cell-Eco in the RNA-based gene expression profiling dataset. Alongside, survival analysis was applied as previously described to the list of differentially expressed genes ($p < 0.05$ and |log2FC|>0.25) between Cell-Eco1 and 2, to identify genes with potential prognostic power.

Quantification and statistical analysis

Statistical analyses were conducted on R (v4.1.1) and GraphPad Prism (v10). Pearson correlations were performed with the R package Hmisc. Differences in cell type proportions between groups were assessed by the non-parametric Kruskal–Wallis test with Dunn's post hoc test.

The Wilcoxon-rank sum test with Bonferroni analysis was applied to identify genes that were differentially expressed between groups. Survival analysis was performed by utilizing Kaplan–Meier curves

with a log-rank test for significance. *P*-values or adjusted *p*-values below 0.05 (<0.05) were considered statistically significant for every test. When not provided as numbers, *p*-values are represented by range: ns (non-significant) > 0.05, * < 0.05, ** < 0.01, *** < 0.001, **** < 0.0001. Statistical methods and parameters are detailed in the figure legends.

Immunofluorescence staining and image analysis

Slides were deparaffinized, rehydrated, and subjected to antigen retrieval in alkaline buffer. After permeabilization, the tissues were incubated overnight at 4 °C with primary antibodies in blocking buffer, followed by secondary antibody incubation for 2 h at room temperature (Table S11). Nuclei were counterstained with DAPI, and slides were mounted with antifade reagent. Confocal images were acquired using a Zeiss LSM 800 microscope and analyzed via Fiji (ImageJ2). Immune cell subsets (CD3+, CD8+, CD20+, CD68+) were quantified relative to DAPI+ nuclei using StarDist-based segmentation.

Results

Spatially-resolved transcriptomic profiles categorize DLBCL tissues by immune cell infiltration and co-localization patterns

We profiled gene expressions with morphological context in a total of 10 DLBCL and 4 secondary lymphoid organs (SLO) tissue sections from formalin-fixed, paraffin-embedded (FFPE) blocks, using Visium Spatial Gene Expression technology from 10x Genomics (Figure 1A). This technology allows the spatial mapping of tissues as 55 µm spots with associated transcriptomic information.

DLBCL samples were collected from eight different patients, six pre-treatment biopsies from different individuals, two longitudinal biopsies (pre- and post-R-CHOP) from one patient, and two pre-treatment biopsies from another individual (n = 10 total; Table S1). As this pilot study focuses on spatial niches rather than patient-level comparisons, each biopsy was considered an independent observation; samples from the same patient or from relapse patients were retained to capture intra-patient spatial heterogeneity. Additionally, two adjacent sections from a reactive lymph node (rLN) and two from a non-metastatic tonsil were included as SLO controls.

First, to profile intra-spot immune cell composition, we integrated public single-cell RNA sequencing data (scRNA-seq)[8,9] (Table S2), with our in-house generated spatial transcriptomics (ST) data used to deconvolute the cell-type mixtures present in each spot (Figure 1A). scRNA-seq data from the CD45+ compartment of DLBCL and SLO tissues were manually curated and annotated based on well-established markers in the literature (Figure S1A, S1B, S1C, S1D and Table S3) and irregular copy number variation (Figure S1F). Cell-type decomposition (RCTD),[16] was performed for spatial transcriptomics integration-based deconvolution to obtain the cell type proportions assigned to each individual spot (Figure 1A, Figure S1E and S1G; Figure S2A).

The robustness of RCTD decomposition was assessed on control tissue, cross-comparing RCTD output (Figure S1G), with spot-cluster annotation (Figure S1H and S1I) and the expert-reviewed histological annotation from SLO (Figure S1J). Both DEGs per cluster and decomposed cell subsets proportions were aligned with the histological annotation, as well as with the gene expression profiles previously described for each anatomical region.[21-23] To validate the tissue topology at the protein level, we conducted immunofluorescence staining for selected markers representing major immune cell types on adjacent sections used for ST (Figure S2B). We observed that RCTD-identified cell types spatially matched the fluorescence patterns of CD20, CD3, and CD68 markers (Figure S2A and S2B), with correlated cell frequencies at the protein level (Figure S2C).

Subsequently, we investigated the spot-based proportions of deconvoluted immune cells across control and DLBCL samples. Eleven populations of immune cells were identified, including malignant B cells, non-malignant B cells, conventional dendritic cells (cDCs), plasmacytoid dendritic cells (pDCs), macrophages, natural killer cells (NK cells), plasma cells, regulatory T cells (Tregs), follicular T helpers (Tfh), CD4+ T cells (T CD4), CD8+ T cells (T CD8). Immune cell proportions varied considerably across patients (Figure 1B and Figure S2D), confirming the heterogeneity of DLBCL.

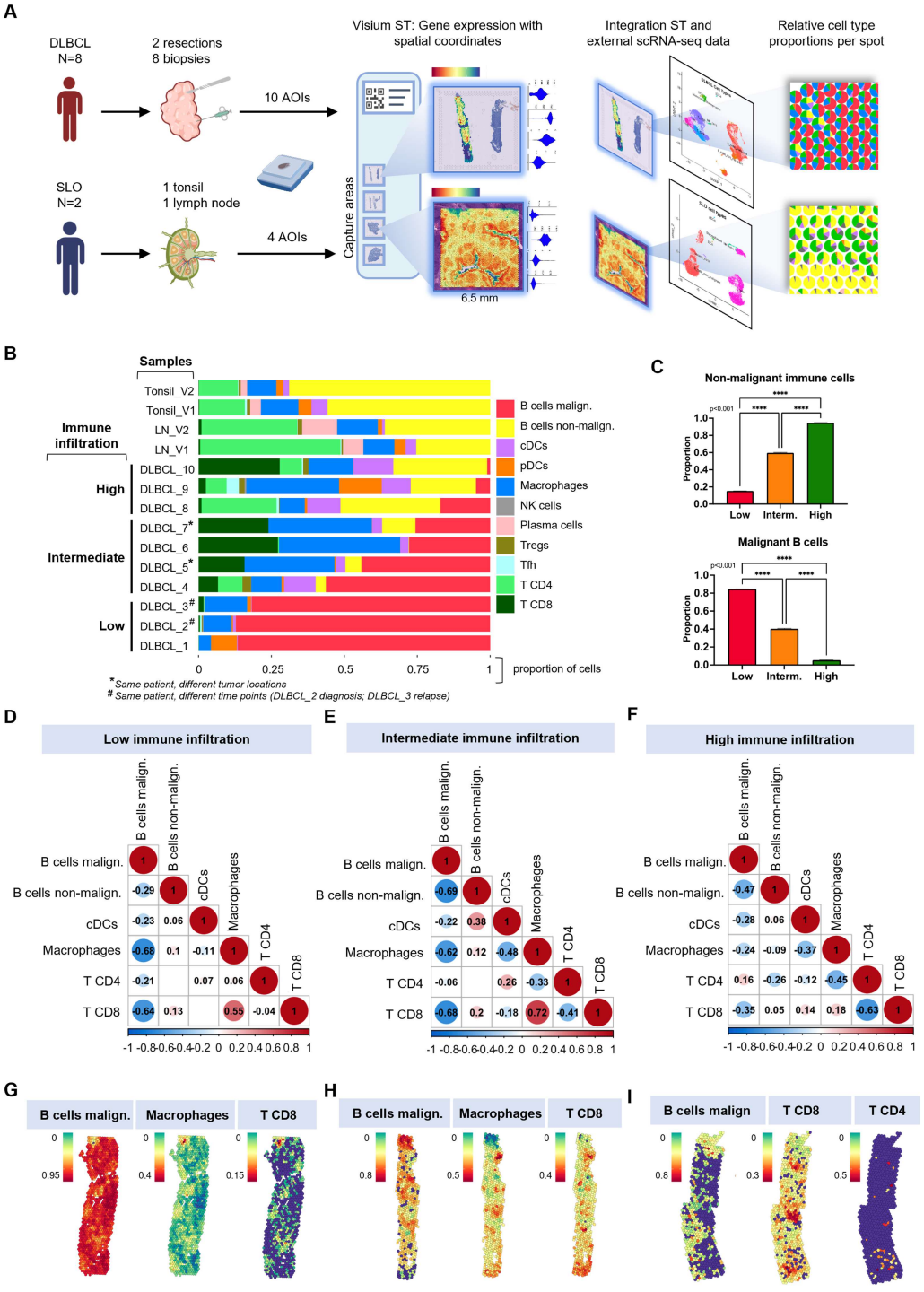

Figure 1. Spatially resolved transcriptomic profiles classify DLBCL tissues by their level of immune cell infiltration with distinct co-localization patterns. (A) A schematic workflow of ST data generation with Visium (10X Genomics). All the samples were formalin-fixed and embedded in paraffin. After RNA quality control, the samples were placed in Visium Spatial slides, which include 4 capture areas of 6.5×6.5 mm^2, with 5000 barcoded spots. ST sequencing results are a matrix of gene counts and coordinates, which are translated into gene expression profiles with a morphological context. Single-cell reference data from publicly available datasets are annotated and integrated with ST data to perform spot deconvolution, providing the relative cell type proportions per spot. (B) Bar plot representing the mean proportions of RCTD-deconvoluted immune cell-types per ST sample. DLBCL ST samples are divided into 3 groups based on their non-malignant immune infiltration. Statistical differences of cell-type proportions across samples are represented in Figure S3D. (C) Mean comparison of malignant B cells proportions (above) and non-malignant immune cells (below) per DLBCL sample group. The immune infiltrate compartment is represented as the sum of the mean relative cell-type proportions other than malignant B cells from the RCTD deconvolution outputs. Multiple comparisons were performed

(*Caption on next page*)

using Kruskal–Wallis statistical test and Dunn's post-hoc (****$p < 0.0001$). (D–F) Intra-spot cell-type colocalization patterns per DLBCL sample group. The color intensity and circle size represent the Pearson correlation coefficients: red indicates positive correlations and blue indicates negative correlations. Only significant correlations ($p < 0.05$) are shown. (G–I) Deconvoluted proportions of general immune cell types in one representative DLBCL ST sample from the low (G), intermediate (H), and high (I) immune infiltrated groups.

Based on tertiles of immune cell proportions (tertile 1 = 0.4362144, tertile 3 = 0.7433377), we grouped the DLBCL samples into low-, intermediate-, and high-infiltration categories. Malignant B cell abundance was inversely correlated with immune cell infiltration (Figure 1C).

Correlation analyses of cell-type frequencies revealed that malignant B cells showed negative or no correlation with most immune cell types, indicating potential mechanisms of immune evasion (Figure 1D, 1E, and 1F). For low- and intermediate-immune cell infiltrated samples, CD8+ T cells and macrophages displayed a significant spatial correlation, suggesting co-localization patterns. Interestingly, the presence of these cells was anticorrelated with malignant B cells, suggesting immune cell niches within the tumor microenvironment (Figure 1D, 1E, 1G, and 1H). In high-infiltrated samples, CD4+ T cells were more prevalent and negatively correlated with CD8+ T cells and macrophages, highlighting distinct cellular co-occurrence arrangements in the tissue (Figure 1F and 1I).

Immune cells are distributed into cellular ecosystems with different neighborhood characteristics

To characterize spatial identities based on colocalization patterns, we used the Leiden algorithm, an improved version of Louvain unsupervised clustering[17] on 7824 spots from ten DLBCL samples (Figure 2A). We identified six clusters defining niches or cellular ecosystems (Cell-Eco) characterized by distinct cellular compositions and abundances across samples (Figure 2A and 2B; Figure S3A; Table S4). As expected, Cell-Ecos with a higher proportion of malignant B cells (Cell-Eco 1 and 2), were more frequent among the low-immune infiltration samples (Figure S3A and S3B). Cell-Eco 3 showed its highest abundance in intermediate immune infiltration group (Figure S3B). In contrast, Cell-Eco 4, 5 and 6 were present at higher frequencies in highly immune infiltrated samples (Figure S3B). Notably, Cell-Eco 4 was the only Cell-Eco with significant presence of CD4+ T cells, together with both malignant and non-malignant B cells, which could be reminiscent of the healthy lymph node cellular composition. Cell-Eco 5 and 6 included non-malignant B cells together with CD8+ T cells and macrophages, but differed in that Cell-Eco 6 also contained conventional dendritic cells (cDCs) (Figure 2B; Figure S3A).

The cellular ecosystems define common identities among spots, which represent spatial units of cells that share coordinates in the ST gene count matrix. However, they also exhibit specific distributions across the tissue section. We studied the compartmentalization of sample groups by analyzing their Cell-Eco neighboring patterns. For that purpose, we calculated a neighbor score based on the relative frequency of Cell-Eco in the direct vicinity by pairs and then determined the mean neighbor scores per sample group (Figure 2C–E). We observed that in low-infiltrated samples, malignant B cell-rich spots (Cell-Eco 1 and Cell-Eco 2) form aggregates not only at the spot level (Figure 1D–F) but also at a broader scale, as indicated by their higher neighbor score (Figure 2C). The high neighbor score of Cell-Eco 3 for the intermediate infiltration group of samples can be attributed to their group-specificity and abundance, which likely contributes to their spatial proximity (Figure 2B and 2D; Figure S3B). Cell-Eco 4 displays great aggregation scores (0.16) in the high-infiltrated group, which could also refer to their abundances (Figure 2E). Notably, Cell-Eco 5 and 6 are the ecosystems in both intermediate and high immune infiltration groups that showed a high dispersion pattern, as indicated by their low mean neighbor scores among different pairs (Figure 2D and 2E). Overall, these data indicate that different Cell-Eco values exhibit distinct neighboring patterns, revealing compartmentalization based on the cellular composition of DLBCL tissue samples.

Interestingly, two biopsies (DLBCL_5 and DLBCL_7) from different tumor locations in the same patient (p04), collected prior to R-CHOP treatment, consistently showed high frequencies of Cell-Eco 3 and clustered in the same group, indicating similar cellular composition across sites. (Figure 1B, Figure S3C, Table S4). Conversely, biopsies from patient p02 (DLBCL_2 and DLBCL_3), collected 232 d apart before and after R-CHOP treatment, showed distinct Cell-Eco profiles. At relapse, DLBCL_3

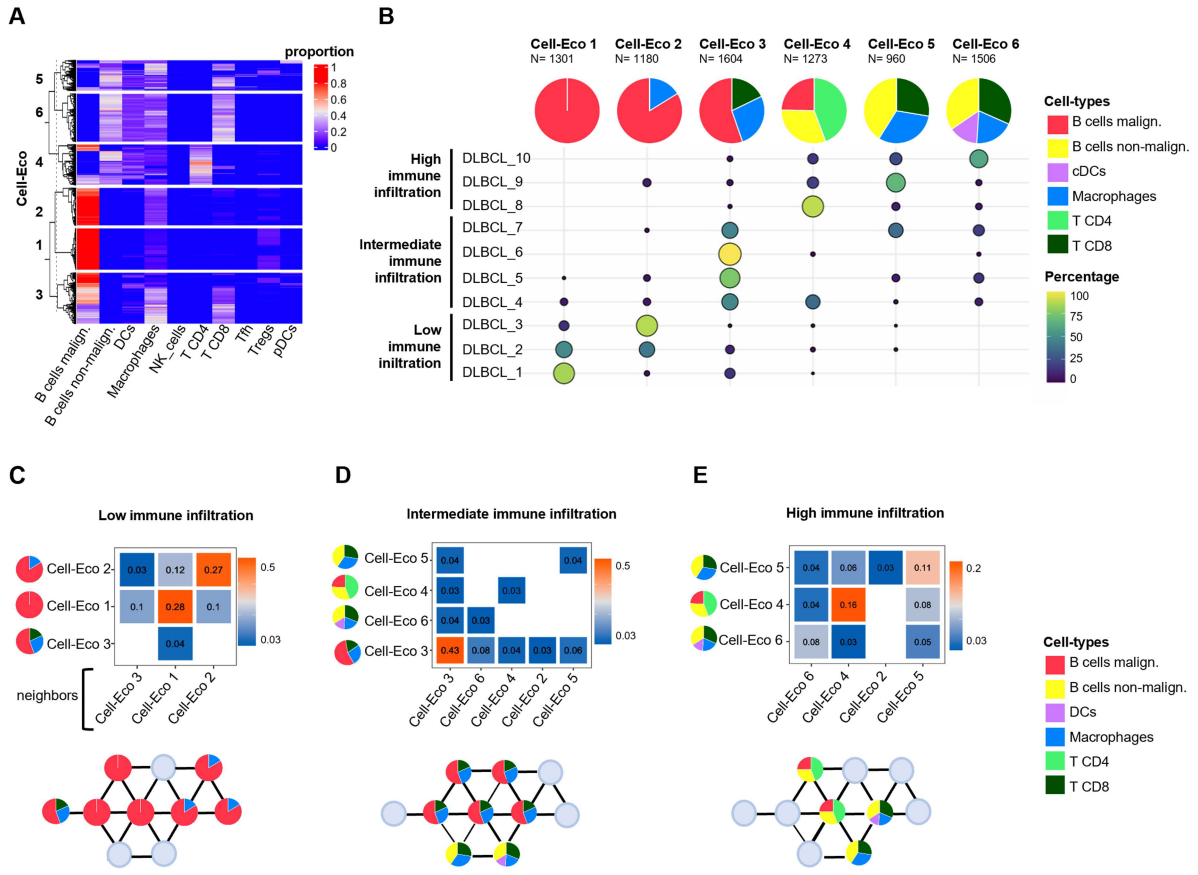

Figure 2. Cellular ecosystems and neighborhood characteristics in DLBCL tumor microenvironment. (A) Heatmap of deconvoluted cell-type proportions per spot of 10 ST DLBCL samples, clustered with the Leiden algorithm (resolution 0.2). (B) Above: pie charts representing the mean cell-type proportions of each Leiden cluster (Cell-Eco). Proportions lower than 10% were excluded from the analysis, and means were scaled to sum 100% per Cell-Eco. Below: bubble plot indicating the percentage of each Cell-Eco per sample. (C–E) Heatmaps of the mean neighbor scores (above) of the Cell-Eco pairs with their schematic representation (below) of samples from the low (C), intermediate (D), and high (E) immune infiltration groups. The heatmap represents the mean neighbor score values; high values are in orange, and low in blue. Only scores higher than 0.03 are represented. Schemas represent Cell-Eco neighboring frequencies based on the scores, in a virtual area of 10 spots. The gray dots indicate negligible neighbor presence.

showed an increased frequency of Cell-Eco 2 (86.24%) compared to baseline (41.08%), suggesting ecosystem remodeling post-treatment (Figure 1B, Figure S3C, Table S4).

Cellular ecosystem signatures allow the stratification of DLBCL patients with different overall survival scores

To evaluate whether spatially resolved Cell-Eco signatures hold a potential prognostic value for DLBCL patient outcomes, we performed survival analysis on a large publicly available RNA-based gene expression profiling dataset. The dataset from the Haematological Malignancy Research Network (HMRN)[24,25] included gene expression information from biopsy samples collected from n = 1149 DLBCL patients, who had survival information over a period of 150 months.

We scored Cell-Eco gene signatures from the ST data, based on differential expression analysis, and clustered patients based on RNA profiling data and Cell-Eco signatures (Table S5). Higher scores for Cell-Eco 1 and Cell-Eco 2 were associated with shorter overall survival (OS) compared to those with a higher proportion of immune cell-types (Figure 3A). We observed notable differences in the Cell-Eco signature scores across clinical variables (Figure S4, Table S6). Patients with activated B cell DLBCL (ABC) molecular subtype, linked to poorer outcomes, had higher Cell-Eco 1 and lower Cell-Eco 2 scores. In

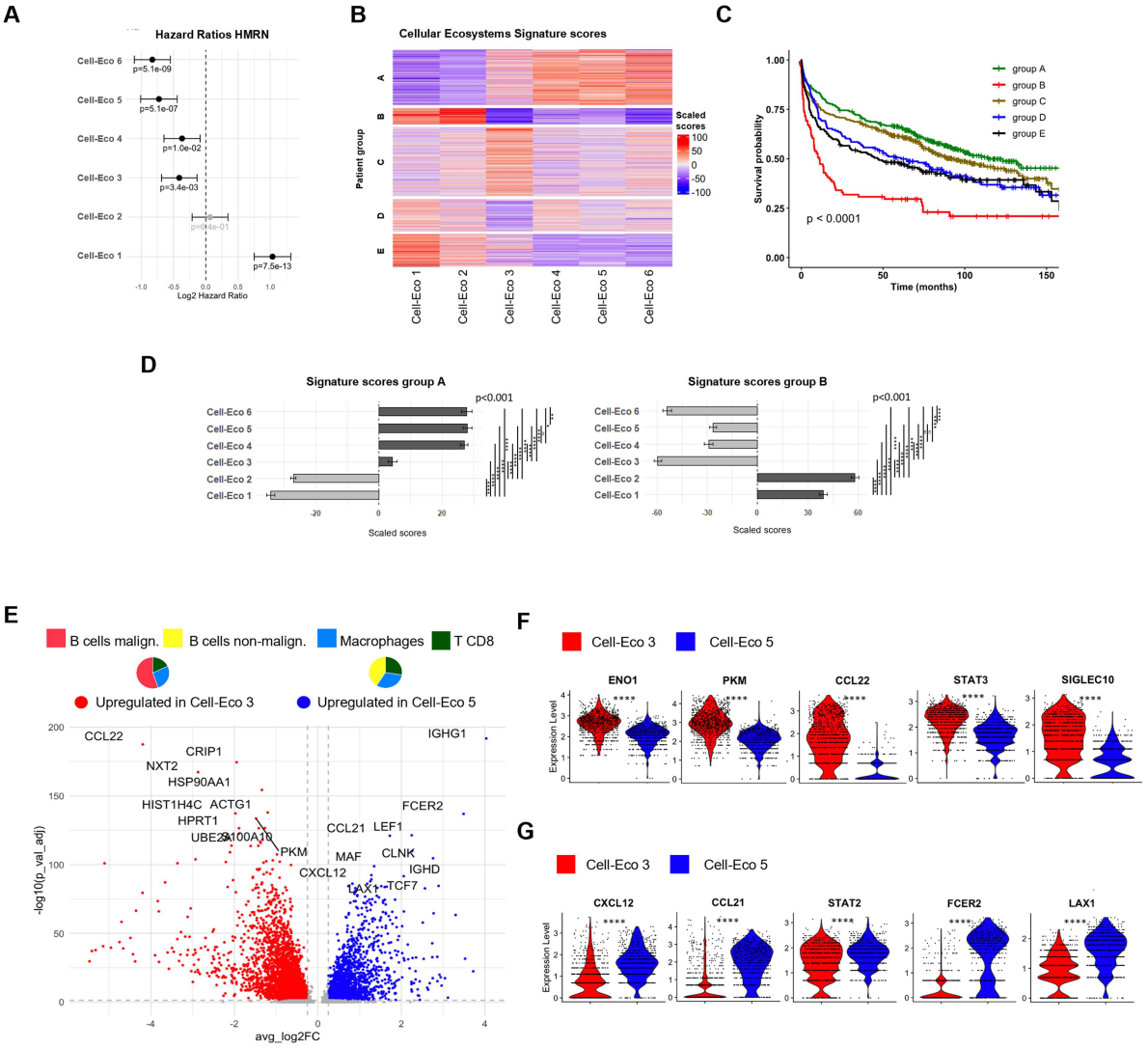

Figure 3. Cellular ecosystems signatures allow patients stratification with different overall survival in DLBCL datasets. (A) Forest plot depicting the univariate Cox proportional hazards model analysis comparing Cellular Ecosystems signatures scores in the DLBCL RNA expression profiling HMRN cohort (n = 1149). (B) Heatmap of patient stratification based on Cellular Ecosystems signature scores in the HMRN cohort, revealing five distinct clusters or patient groups (A = 310, B = 91, C = 387, D = 179, E = 182). (C) Kaplan–Meier curves showing the overall survival of the patient clusters from Figure 4C, showing the p-value from the log-rank test. (D) Bar plots of the Cell-Eco signature scores for individual patient groups A and B. Multiple comparisons were performed using Kruskal-Wallis statistical test and Dunn's post-hoc. (E) Volcano plots showing differentially expressed genes between Cell-Eco 3 (in red) and Cell-Eco 5 (in blue), based on log2FC > 0.25 and adjusted p-value < 0.05. P-values were determined by the Wilcoxon rank-sum tests. Labels of the top 10 genes with lower adjusted p-values are displayed in the plot. (F, G) Violin plots showing genes differentially upregulated in Cell-Eco 3 (F) and Cell-Eco 5 (G).

contrast, patients classified as germinal center B cell DLBCL (GCB) phenotype showed elevated Cell-Eco 2 and 3 scores and lower scores for non-malignant ecosystems (Figure S4A). Other Cell-Eco signature score patterns appeared across LymphGen subtype classifications[26] and IPI scores, revealing the impact of Cell-Eco on clinical characteristics (Figure S4B and S4C).

These scores enabled the stratification of patients from the HMRN[24,25] cohort into five distinct groups (A–E; Figure 3B), each with different survival outcomes (Figure 3C). Group A had the highest OS and was enriched in immune cell-rich Cell-Ecos (Figure 3C, D). Group C, which was also associated with better OS, had higher Cell-Eco 3 scores (Figure S4D). On the other hand, patients with the poorest OS belonged to group B, with high scores for malignant Cell-Ecos and negative scores for immune-rich Cell-Ecos (Figure 3C, D).

Interestingly, Cell-Eco 3 and 5 present similar cellular compositions but differ in the malignancy status of B cells. To further explore their transcriptomic differences, we conducted a differential gene expression analysis, revealing a strong glycolytic profile in malignant Cell-Eco 3 (ENO1, PKM, STM1, and CDK1) cells (Figure 3E and 3F; Table S7). This profile has been previously linked to progression and resistance and is upregulated in DLBCL malignant B cells.[21] This Cell-Eco also exhibits higher expression of cell cycle, proliferation (HIST1H4C, NXT2, CRIP1), and cell motility genes (ACTG1, ACTB),[27] compared to Cell-Eco 5 (Figure 3E and 3F; Table S7). In addition, we noted a significant upregulation of CCL22 in Cell-Eco 3 (Figure 3F), a chemokine produced by tumor-associated macrophages, which has been linked to tumor metastasis and reduced patient survival.[28] Other genes highly expressed in Cell-Eco 3 included genes associated with anti-inflammatory signaling[29] such as STAT3, SIGLEC10, and CD24 (Figure 3E and 3F; Table S7). Conversely, Cell-Eco 5 associated with higher expression of immune cell recruitment genes (CXCL12, CCL21 and CCL19) and IFN-induced transcription factors (STAT2, STAT4), together with genes associated with macrophage functions (FCER2, MAF) as well as T cell differentiation and functions (LAX1, TCF7, CD40LG, ILR7)[30] (Figure 3E and 3G; Figure S4E; Table S7). Altogether, these findings underscore the importance of assessing the biological mechanisms involved in each cellular ecosystem, beyond their immune cell composition.

Tumor-supportive macrophages are the predominant cell type in direct contact with malignant B cells and shape the DLBCL tumor microenvironment spatial architecture

To investigate the role of macrophages in highly malignant Cell-Eco, we performed differential gene expression analysis (DEA) between Cell-Eco 1 and Cell-Eco 2, which are both rich in malignant B cells but differ in their macrophage content (Figure S3A). We observed that 2332 and 4473 genes were significantly upregulated in Cell-Eco 1 (B cells malignant mean $_{\text{Cell-Eco 1}}$ = 100%) and Cell-Eco2 (B cells malignant mean $_{\text{Cell-Eco 2}}$ = 83.68%, macrophages mean $_{\text{Cell-Eco 2}}$ = 56.82%), respectively, highlighting differences in gene expression profiles (Table S8).

Cell-Eco 1 presented a transcriptomic profile of malignant B cells, which was supported by the DisGeNET enrichment analysis (Figure S5A). Cell-Eco 1 also presented significantly higher expression of genes associated to B cell memory and plasma cells (TNFRSF13B, IGHM, IGHG3, CCR7, IL10RA, IRF4, PRDM1, and JAK1) (Figure 4A and 4B), indicating a post-GC differentiation status.[27,31] We observed upregulation of germinal center dark zone-related genes (MS4A1 and FOXP1),[26] B cell survival and proliferation (IL10, IFR4, MYD88, JAK1, STAT3, BCL2, and CD72),[32-34] anti-apoptotic activity (SPIB),[29] immune attraction (CCL22 and CCR4),[35] glycolysis (ENO2, STMN1, PKM, and CDK5R1)[36] and motility (ACTG1, ACTG2, and CD37)[30] which are characteristics commonly associated with B cell malignancies (Figure 4A and 4B). Notably, cell–cell communication analysis based on ligand–receptor interactions using ICELLNET[37] framework revealed higher communication scores related to B cell immunosuppressive activities in Cell-Eco 1 (GZMB, CD52, and IL16)[38-40] (Figure 4B and 4C).

Consistent with the presence of macrophages in Cell-Eco 2, Cell-Eco exhibited an upregulation of macrophage lineage genes (Table S8), which was supported by pathway enrichment analysis (Figure S5B). In addition, macrophage infiltration into the malignant microenvironment was confirmed by applying module scores of the germinal center (GC) vs inter-follicular (IF) macrophage signatures (MacroSig) from Lui et al.[13] The macrophages from Cell-Eco2 group presented a higher score of GC signatures compared to lymph node control macrophages (Figure S5C). Interestingly, Cell-Eco 2 spots showed enrichment in genes related to metabolic activity and antigen presentation, alongside markers of the immunosuppressive C1q+ macrophage phenotype, the anti-inflammatory M2 marker IL4I1, and the proto-oncogene BCL6, which are associated with poor prognosis (Figure 4A, 4C and 4D; Table S8).[33,34] Ligand-receptor analyses identified communication pathways associated with the downregulation of macrophage anti-tumor activity (LGALS1-LGALS1, APP-CD74, and CXCL12-CCR4), supporting tumor-associated macrophage infiltration (Figure 4C).

We then investigated whether Cell-Eco 1 and Cell-Eco 2 are linked to clinical outcomes. To do this, we conducted survival analyses using external RNA profiling datasets. Among the 561 DEGs with survival significance in two independent datasets: HMRN[24,25] and Visco et al.[41] (Table S9, Figure 4E), we identified genes upregulated in Cell-Eco 1 that were significantly associated with worse prognosis, such as PIM1 and

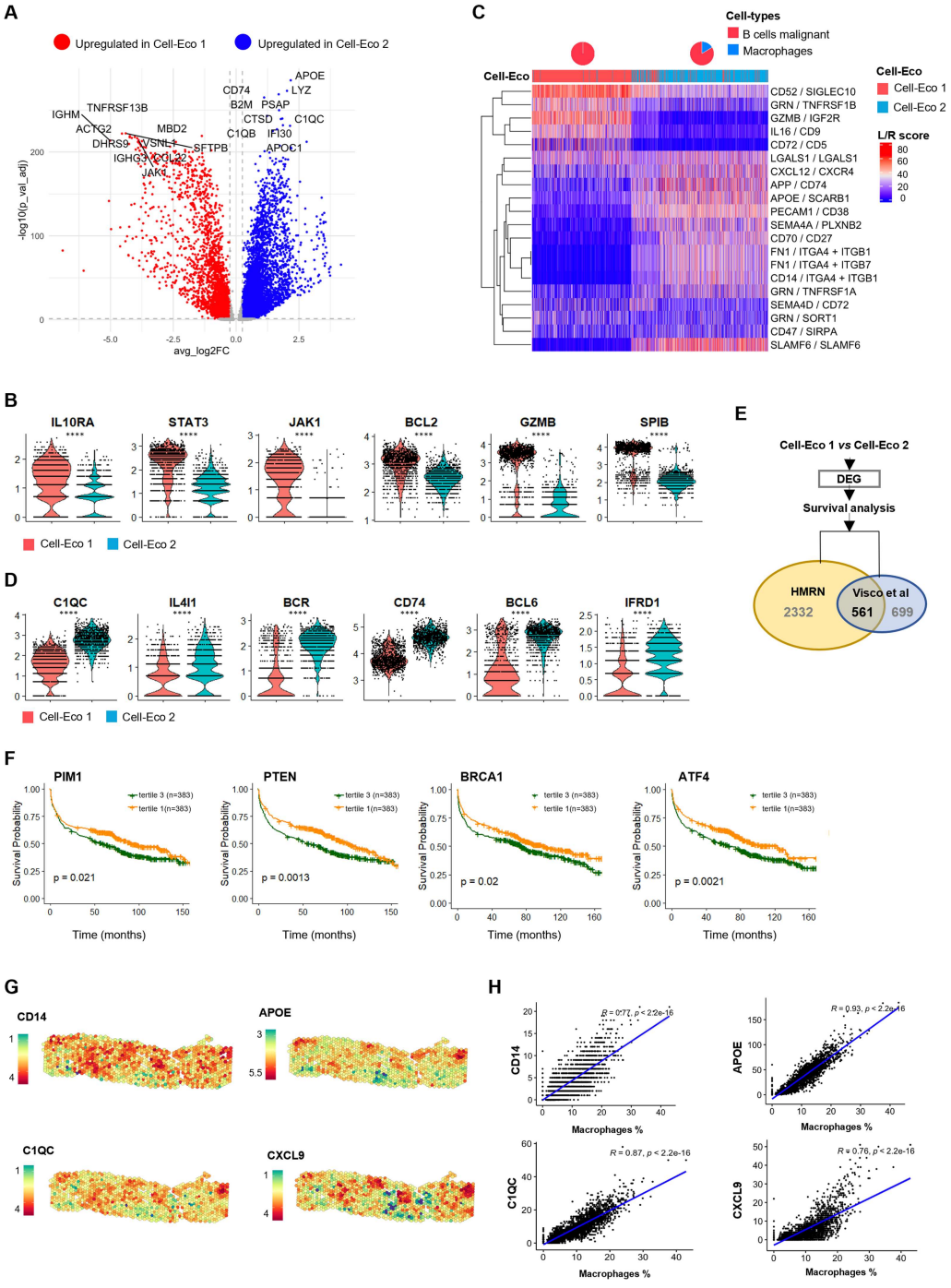

Figure 4. Tumor-supportive macrophages are the predominant cell type in direct contact with malignant B cells and shape the DLBCL tumor microenvironment spatial architecture. (A) Volcano plot showing the DEGs between Cell-Eco 1 (in red) and Cell-Eco 2 (in blue), based on log2FC > 0.25 and adjusted *p*-value < 0.05. *P*-values were determined by the Wilcoxon rank-sum tests. The labels of the top 10 genes with lower adjusted *p*-values are displayed in the plot. (B and D) Violin plots showing genes differentially upregulated in Cell-Eco 1 and Cell-Eco 2 (log2FC > 0.25 and adjusted *p*-value < 0.05 from the Wilcoxon-rank sum tests). (C) Heatmap of ligand/receptor interaction scores based on intra-spot gene expression, between Cell-Eco1 (mean malignant B cell = 100%) and Cell-Eco 2 (mean malignant B cells = 83.68, mean macrophages = 16.32%). (E) Venn diagram illustrating the intersection of significant genes for survival analysis in two datasets of DLBCL RNA-based gene expression profiling. Genes were considered significant if the log-rank test *p*-value was below 0.05. The input for the survival analysis was DEGs between Cell-Eco 1 and Cell-Eco 2 (log2FC > 0.25 and adjusted *p*-value < 0.05 from the Wilcoxon rank-sum tests). (F) Kaplan–Meier curves with long-rank test *p*-value showing overall survival of patients divided by tertiles 1 and 2 for specific gene expression in the HMRN cohort. (G) Spatial representation of gene expression organization of spatially auto-correlated genes on a representative ST DLBCL sample. (H) Scatter plots representing correlations between gene expression of spatially autocorrelated genes and the percentage of macrophages deconvoluted per spot in low infiltrated group of DLBCL ST samples. *P*-values from Pearson correlation.

PTEN[37] (Figure 4F; Figure S5D). On the other hand, Cell-Eco 2 shows upregulation of tumor suppressor genes such as BRCA1 and genes involved in metabolic pathways essential for DLBCL survival, such as ATF4.[38] This finding suggests that malignant B cell-rich Cell-Eco may use different escape mechanisms based on their cellular composition and functions.

Spatial autocorrelation analysis based on Moran's I statistics[39] identified 210 genes with similar expression levels in spatially proximate spots within the tissue[40] in the low infiltration group of samples (Table S10). Interestingly, 39 of these genes showed positive and significant correlation ($R > 0.5$, $p < 0.05$) with macrophage frequencies but no correlation with malignant B cells (Figure 4G and 4H; Figure S5E). This suggests that tumor-associated macrophages may play a role in the spatial organization and cellular remodeling of the TME in DLBCL, potentially facilitating immune evasion by malignant B cells.

Discussion

Next-generation sequencing (NGS) analysis of the tumor microenvironment (TME) in DLBCL has shown a link between immune cell infiltration and patient prognosis.[8,41,42] However, integrating spatial information with large-scale immune profiling in DLBCL has been challenging due to its diffuse architecture.[10,15,21] Here, spatial transcriptomics reveals spatially restricted gene expression programs within the DLBCL TME.

While spatially defined composite cell neighborhoods (CNT) have been previously described by Wright et al.[10] using a 27-plex Multiplex Ion Beam Imaging (MIBI) panel, our study employed unsupervised clustering, independently of predefined panels. Our analysis identified six distinct immune cellular ecosystems (Cell-Eco) within the DLBCL TME, defined by unique cellular composition, communication patterns, and neighborhood characteristics. These Cell-Eco capture both immune composition and infiltration patterns. Indeed, in line with Wright et al. findings, we observed that Cell-Eco varied in proportions of tumor and immune cells, that were inversely correlated. Similarly, our findings align with the cellular niches (CN) defined by Dai et al.[42] using CosMx spatial transcriptomics; they highlight that structurally distinct immune neighborhoods characterize the phenotypic and spatial heterogeneity of the DLBCL microenvironment architecture. Importantly, we demonstrated that these Cell-Eco have significant prognostic potential, as their gene signatures stratify DLBCL patients by overall survival (OS) in independent datasets,[25] emphasizing the need for Cell-Eco-specific analyses to understand their biological and clinical significance.

One notable finding is the characterization of Cell-Eco 4, which is abundant in highly infiltrated samples and characterized by a significant proportion of CD4+ T cells. Higher $CD4^+$ T-cell abundance was associated with improved post-treatment survival.[5,8] In Cell-Eco 4, CD4+ T cells share coordinates with non-malignant B cells, which could reflect a reminiscence of healthy lymph node tissue. Conventional dendritic cells (cDCs), which are key players in antigen presentation, were detected only in Cell-Eco 6, the ecosystem with the most diverse immune cell infiltration. Contrary to the previous study from Wright et al.[10] we found cDCs and macrophages co-occurring within the same spots. Notably, cDCs were more frequently associated with immune cells than with malignant B cells, suggesting a potential role in immune coordination.

Survival analysis revealed that the Cell-Eco holds different prognostic potentials, with immune-rich niches associated with a more protective effect. This aligns with the "hot and cold" tumor paradigm.[43] However, our study provides spatially resolved insights based on deep transcriptomics analysis of these cellular colocalizations. Moreover, Cell-Eco signatures can stratify patients by overall survival, indicating that individual Cell-Eco and their combinations influence prognosis and reflect the heterogeneity of DLBCL. Cell-Eco signature scores vary across clinical subgroups, with Cell-Eco1 being more prevalent in the activated B-cell-like (ABC) DLBCL subtype, while Cell-Eco2 has a higher score in the GCB subtype, and vice versa. Variations in Cell-Eco scores across molecular subtypes, LymphGen classes, and IPI scores further highlight their clinical relevance, suggesting that these ecosystems impact not only survival but also other key clinical characteristics.

A remarkable result our ST analysis derives from the comparison between Cell-Eco 3 and Cell-Eco 5, both containing CD8+ T cells and macrophages but differing in the malignant status of B cells. Despite similar cell composition, these ecosystems exhibit distinct transcriptomic profiles. For instance, Cell-Eco 3

exhibits upregulation of CCL22, a chemokine involved in Tregs recruitement[44] and immune evasion in various cancer types, including DLBCL.[43] In addition, CCL22 expressed by M2 macrophages has been associated with metastasis and drug resistance, highlighting its potential as a therapeutic target for patients with high Cell-Eco 3 signatures. Another interesting finding is the upregulation CD24/SIGLEC10 communication axis in Cell-Eco 3 compared to Cell-Eco 5. While monoclonal antibody therapy targeting CD24 in DLBCL has shown limited efficacy,[24] our results suggest that targeting this axis should be restricted to patients with a high Cell-Eco 3 score.

In addition, we observed that Cell-Eco 3 presents a high glycolytic profile coupled with upregulation of anti-inflammatory signaling like STAT3, a component of the JAK/STAT signaling pathway involved in lymphomagenesis and tumor progression[45] upregulated in ABC DLBCL cells[338]. Interestingly, a recent study by Dai et al.[35] identified clusters of malignant B cells and TAM (Tumor Associated Macrophages) presenting a similar glycolytic profile within an exhausted immune microenvironment. These differences highlight the clinical importance of assessing cellular ecosystem functions beyond cell composition.

Our analysis also sheds light on the role of macrophages in DLBCL, which have been associated with poor clinical outcomes in several studies.[46-48] Recently, Liu et al.[13] identified distinct macrophage signatures with prognostic significance in DLBCL. To characterize the macrophages in direct proximity to malignant B cells, we performed differential expression analysis (DEA) between Cell-Eco 1 and Cell-Eco 2, differing only by the presence of macrophages.

This analysis revealed that Cell-Eco 1 (composed mainly of malignant B cells) expresses markers associated with B cell activation, proliferation, and metastasis. Nevertheless, the higher expression of markers such as IL10, CD52, IL16, and GZMB reflects the immunosuppressive functions of malignant B cells in this Cell-Eco. Interestingly, GZMB-producing B cells have been described to suppress T cell proliferation and cytokine production in different cancer types and lymphoma cell lines.[49,50] Thus, GZMB-producing malignant B cells may contribute to T cell exclusion in ecosystems rich in malignant B cells.

In contrast, Cell-Eco 2 (composed of malignant B cells together with macrophages) exhibits upregulation of macrophage lineage genes associated with the C1q+ subpopulation.[51] This phenotype goes beyond the M1/M2 dichotomy, suggesting a possible role of the complement pathway in macrophage polarization and tumor proliferation in this Cell-Eco. Enrichment in complement recognition patterns by macrophages was associated with poorer survival in a recent study from Liu et al.[13] Dai et al. reported enrichment of C1Q+ macrophages in immune-privileged niches of EBV-positive DLBCL.[35] Another study revealed that C1QB-expressing macrophages are the source of cholesterol efflux linked to CAR-T resistance in refractory DLBCL.[52] These findings underscore the significance of complement activation and metabolic pathways for macrophage activity, highlighting their potential role in DLBCL treatment response. Notably, Cell-Eco 2 was the most abundant in sample DLBCL_3, the only sample analyzed post-relapse from R-CHOP treatment. This suggests a shift in the cellular composition and colocalization after treatment, with macrophage phenotype potentially serving as an indicator of treatment response.

Moreover, in samples with high malignant B cell proportions, macrophage levels correlated with spatially restricted gene expression, suggesting that macrophages may play a key role in organizing highly malignant microenvironments. Other spatially restricted genes were linked to stromal cells, especially cancer-associated fibroblasts (CAFs), which we did not analyze because of limitations in the available scRNA-seq datasets. These stromal cells may play a key role in orchestrating immune cell infiltration within the TME.

This study has several limitations, including a small sample size and limited tissue coverage. Although Cell-Eco patterns were consistent across biopsies from the same patient, larger cohorts are needed to fully characterize DLBCL spatial heterogeneity. As a discovery cohort, our study serves as a pilot effort to generate mechanistic insights into the spatial organization of the DLBCL tumor microenvironment.

Conclusion

This spatial transcriptomic study expands the understanding of DLBCL tissue architecture, revealing novel cellular organizations, cell states, and communication patterns organized into distinct cellular ecosystems. Importantly, the clinical relevance of these cellular ecosystems was validated by the stratification of patients based on overall survival using external public datasets. Beyond identifying cell type phenotypes,

our study stresses the need for a deep characterization of cell–cell interactions and functional states at the spot-level, to better understand the TME dynamics and clinical outcomes in DLBCL. Finally, this study provides a valuable data resource for further in-depth analysis of the TME in DLBCL and the identification of potential therapeutic targets or biomarkers.

Disclosure of potential conflicts of interest

A.D.H. was supported by a PhD fellowship from Servier. L.M.R. is currently employed by Mnemo Therapeutics. V.S. is currently employed by Owkin. The remaining authors declare no competing interests.

Acknowledgments

We thank the Institut Curie PATHEX and NGS facilities, in particular Renaud Leclere, and Mylene Bohec for their technical support. We also thank the Institut de Recherche Saint-Louis imaging facility, in particular to Niclas Setterblad, for their technical support. This article is derived from the first author's doctoral thesis entitled *"Characterization of Tumor Immune Microenvironment in Human Diffuse Large B-cell Lymphoma"*, submitted to the Paris-Saclay University in Paris, France.

A.D.H. conceived the project, built the circuit of samples, analyzed and interpreted the ST data, and wrote the manuscript. H.P.P. performed the tissue staining and quantification of immunofluorescence images and contributed to the manuscript writing. J.L.C. conducted RNA quality control from FFPE tissue sections. L.M.R. and M.V. provided technical and conceptual advice for the bioinformatic analyses and contributed to the scRNA-seq analysis. J.C., C.C., V.M., and C.T. facilitated access to histological samples, clinical information, and interpretation. V.B. and V.S. contributed to the study design, project management, and funding. P.T. contributed to the study design, project management and funding, data interpretation, and supervised the work. All authors reviewed the manuscript.

Funding

This work was supported by the laboratory of excellence (Labex) Inflamex, the Fondation ARC pour la Recherche sur le Cancer (Sys-Can ARCPGA12021 020003101_358 7), and the Institut National de la Santé et de la Recherche Médicale (INSERM) under the grant CHEMOTAXIS IN CANCER. A.D.H. was supported by a PhD fellowship from Servier. L.M.R. was supported by a PhD fellowship from La Ligue Contre le Cancer and Fondation ARC. P.T. is supported by the ATIP-Avenir program from INSERM and CNRS.

Author contributions

CRediT: **Alba Diaz-Herrero:** Conceptualization, Data curation, Formal analysis, Investigation, Methodology, Resources, Validation, Visualization, Writing – original draft; **Héctor Fernando Pelaez-Prestel:** Data curation, Formal analysis, Investigation, Visualization, Writing – original draft; **Lucile Massenet-Regad:** Conceptualization, Data curation, Methodology; **Maëva Veyssiere:** Conceptualization, Data curation, Methodology; **Julien Calvani:** Data curation, Resources; **Caterina Cristinelli:** Data curation, Resources; **Jacqueline Lehmann-Che:** Investigation; **Véronique Meignin:** Data curation, Resources; **Catherine Thieblemont:** Conceptualization, Resources; **Véronique Blanc:** Conceptualization, Funding acquisition, Resources, Supervision; **Vassili Soumelis:** Conceptualization, Funding acquisition, Project administration, Supervision; **Pierre Tonnerre:** Conceptualization, Funding acquisition, Project administration, Supervision, Writing – review & editing.

Data availability statement

The spatial transcriptomics dataset generated for this study has been deposited in Gene Expression Omnibus (GEO) under the accession number GSE276542, which is publicly available for non-commercial use. The scRNA-seq dataset used for spatial data deconvolution was retrieved from heiDATA under accession code VRJUNV and from GEO under accession number GSE182436. The public DLBCL expression array dataset was retrieved from GEO under the accession numbers GSE31312 and GSE181063. The source codes for processing all the datasets are available as a GitHub repository https://github.com/a-diaz-herrero/ST_DLBCL. Any additional data that support the findings of this study are available from the corresponding author upon reasonable request.

Ethical approval statement

Ethical approval for the ImmunoLymph protocol was granted by the Comité Local d'Ethique pour la Recherche Clinique des HUPSSD Avicenne–Jean Verdier–René Muret (CLEA-2020-113). This protocol governs the collection

and research use of biological samples from patients treated within the AP-HP hospital network, including Hôpital Saint-Louis, where the samples analyzed in this study were obtained. Therefore, the appropriate ethics committee is the one that approved the clinical protocol under which the samples were collected, rather than the institutional affiliations of the authors. Written informed consent for the use of biological samples and associated clinical data for research and publication was obtained from all participants prior to inclusion in the study.

References

1. Swerdlow SH, Campo E, Pileri SA, Harris NL, Stein H, Siebert R, Advani R, Ghielmini M, Salles GA, Zelenetz AD, et al. The 2016 revision of the world health organization classification of lymphoid neoplasms. 2016;127, pp. 2375–2390. American Society of Hematology Blood. [cited 2021 Jan 11]. Available from: http://ashpublications.org/blood/article-pdf/127/20/2375/1393632/2375.pdf.
2. Schürch CM, Bhate SS, Barlow GL, Phillips DJ, Noti L, Zlobec I, Chu P, Black S, Demeter J, McIlwain DR, et al. Coordinated cellular neighborhoods orchestrate antitumoral immunity at the colorectal cancer invasive front. Cell. 2020;182(5):1341–1359.e19. doi: 10.1016/j.cell.2020.07.005.
3. Angelo M, Bendall SC, Finck R, Hale MB, Hitzman C, Borowsky AD, Levenson RM, Lowe JB, Liu SD, Zhao S, et al. Multiplexed ion beam imaging of human breast tumors. Nat Med. 2014;20(4):436–442. doi: 10.1038/nm.3488 2014 204. [cited 2024 Apr 17]. Available from: https://www.nature.com/articles/nm.3488.
4. Ji AL, Rubin AJ, Thrane K, Jiang S, Reynolds DL, Meyers RM, Guo MG, George BM, Mollbrink A, Bergenstråhle J, et al. Multimodal analysis of composition and spatial architecture in human squamous cell carcinoma. Cell. 2020;182(2), 497. doi: 10.1016/j.cell.2020.05.039.
5. Ciavarella S, Vegliante MC, Fabbri M, De Summa S, Melle F, Motta G, De Iuliis V, Opinto G, Enjuanes A, Rega S, et al. Dissection of DLBCL microenvironment provides a gene expression-based predictor of survival applicable to formalin-fixed paraffin-embedded tissue. Ann Oncol. 2018;29(12):2363–2370. doi: 10.1093/annonc/mdy450.
6. Keane C, Gill D, Vari F, Cross D, Griffiths L, Gandhi M. CD4 $^{+}$ tumor infiltrating lymphocytes are prognostic and independent of R-IPI in patients with DLBCL receiving R-CHOP chemo-immunotherapy. Am J Hematol. 2013;88(4):273–276. doi: 10.1002/ajh.23398.
7. Roider T, Seufert J, Uvarovskii A, Frauhammer F, Bordas M, Abedpour N, Stolarczyk M, Mallm J, Herbst SA, Bruch P, et al. Dissecting intratumour heterogeneity of nodal B-cell lymphomas at the transcriptional, genetic and drug-response levels. Nat Cell Biol. 2020;22(7):896–906. doi: 10.1038/s41556-020-0532-x.
8. Chloé Steen AB, Luca BA, Esfahani MS, Gentles AJ, Newman AM, Alizadeh AA, Azizi A, Sworder BJ, Nabet BY, Kurtz DM, et al. The landscape of tumor cell states and ecosystems in diffuse large B cell lymphoma in brief the landscape of tumor cell states and ecosystems in diffuse large B cell lymphoma. Cancer Cell. 2021;39:1422–1437.e10. doi: 10.1016/j.ccell.2021.08.011.
9. Roider T, Baertsch MA, Fitzgerald D, Vöhringer H, Brinkmann BJ, Czernilofsky F, Knoll M, Llaó-Cid L, Mathioudaki A, Faßbender B, et al. Multimodal and spatially resolved profiling identifies distinct patterns of T cell infiltration in nodal B cell lymphoma entities. Nat Cell Biol. 2024;26(3):478–489. doi: 10.1038/s41556-024-01358-2.
10. Wright KT, Weirather JL, Jiang S, Kao KZ, Sigal Y, Giobbie-Hurder A, Shipp MA, Rodig SJ. Diffuse large B-cell lymphomas have spatially defined, tumor immune microenvironments revealed by high-parameter imaging. Blood Adv. 2023;7(16):4633–4646. doi: 10.1182/bloodadvances.2023009813.
11. Reiss DJ, Nakayama Y, Weng AP, Stokes ME, Sehn L, Steidl C, Scott DW, Huang CC, Gandhi AK. High-plex imaging and cellular neighborhood spatial analysis reveals multiple immune escape and suppression patterns in diffuse large B-cell lymphoma. Leuk. 2024;38(5):1164–1168. doi: 10.1038/s41375-024-02239-1.
12. Colombo AR, Hav M, Singh M, Xu A, Gamboa A, Lemos T, Gerdtsson E, Chen D, Houldsworth J, Shaknovich R, et al. Single-cell spatial analysis of tumor immune architecture in diffuse large B-cell lymphoma. Blood Adv. 2022;6(16):4675–4690. doi: 10.1182/bloodadvances.2022007493.
13. Liu M, Bertolazzi G, Sridhar S, Lee RX, Jaynes P, Mulder K, et al. Spatially-resolved transcriptomics reveal macrophage heterogeneity and prognostic significance in diffuse large B-cell lymphoma. Nat Commun. 2024;15(1):2113. doi: 10.1038/s41467-024-46220-z.
14. Diaz Herrero A, Pelaez-Prestel HF, Massenet-Regad L, Veyssiere M, Calvani J, Cristinelli C, et al. Spatial transcriptomics unveils immune cellular ecosystems associated with patient survival in diffuse large B-cell lymphoma. bioRxiv. 2024. doi: 10.1101/2024.09.16.613252v1.
15. Gao R, Bai S, Henderson YC, Lin Y, Schalck A, Yan Y, Kumar T, Hu M, Sei E, Davis A, et al. Delineating copy number and clonal substructure in human tumors from single-cell transcriptomes. Nat Biotechnol. 2021;39(5):599–608. doi: 10.1038/s41587-020-00795-2.
16. Cable DM, Murray E, Zou LS, Goeva A, Macosko EZ, Chen F, Irizarry RA. Robust decomposition of cell type mixtures in spatial transcriptomics. Nat Biotechnol. 2022;40(4):517–526. doi: 10.1038/s41587-021-00830-w.
17. Traag VA, Waltman L, van Eck NJ. From louvain to Leiden: guaranteeing well-connected communities. Sci Reports. 2019;9(1):1–12. doi: 10.1038/s41598-019-41695-z.

18. Zhou Y, Zhou B, Pache L, Chang M, Khodabakhshi AH, Tanaseichuk O, Benner C, Chanda SK. Metascape provides a biologist-oriented resource for the analysis of systems-level datasets. Nat Commun. 2019;10(1):1523. doi: 10.1038/s41467-019-09234-6.
19. Piñero J, Ramírez-Anguita JM, Saüch-Pitarch J, Ronzano F, Centeno E, Sanz F, et al. The DisGeNET knowledge platform for disease genomics: 2019 update. Nucleic Acids Res. 2020;48(D1):D845–55. doi: 10.1093/nar/gkz1021.
20. Moran PAP. Notes on continuous stochastic phenomena. Biometrika. 1950;37(1/2):17. doi: 10.2307/2332142.
21. Massoni-Badosa R, Aguilar-Fernández S, Nieto JC, Soler-Vila P, Elosua-Bayes M, Marchese D, Kulis M, Vilas-Zornoza A, Bühler MM, Rashmi S, et al. An Atlas of cells in the human tonsil. Immunity. 2024;57(2):379–399.e18. doi: 10.1016/j.immuni.2024.01.006.
22. Stebegg M, Kumar SD, Silva-Cayetano A, Fonseca VR, Linterman MA, Graca L. Regulation of the germinal center response. Front Immunol. 2018;9(OCT):417112. doi: 10.3389/fimmu.2018.02469.
23. Li H, Wang D, Zhou X, Ding S, Guo W, Zhang S, Huang T, Cai Y. Characterization of spleen and lymph node cell types via CITE-seq and machine learning methods. Front Mol Neurosci. 2022;15:1033159. doi: 10.3389/fnmol.2022.1033159.
24. Painter D, Barrans S, Lacy S, Smith A, Crouch S, Westhead D, Sha C, Patmore R, Tooze R, Burton C, et al. Cell-of-origin in diffuse large B-cell lymphoma: findings from the UK's population-based haematological malignancy research network. Br J Haematol. 2019;185(4):781–784. doi: 10.1111/bjh.15619.
25. Lacy SE, Barrans SL, Beer PA, Painter D, Smith AG, Roman E, Cooke SL, Ruiz C, Glover P, Van Hoppe SJL, et al. Targeted sequencing in DLBCL, molecular subtypes, and outcomes: a haematological malignancy research network report. Blood. 2020;135(20):1759–1771. doi: 10.1182/blood.2019003535.
26. Wright GW, Huang DW, Phelan JD, Coulibaly ZA, Roulland S, Young RM, Wang JQ, Schmitz R, Morin RD, Tang J, et al. A probabilistic classification tool for genetic subtypes of diffuse large B cell lymphoma with therapeutic implications. Cancer Cell. 2020;37(4):551–568.e14. doi: 10.1016/j.ccell.2020.03.015.
27. Witjes L, Van Troys M, Verhasselt B, Ampe C. Prevalence of cytoplasmic actin mutations in diffuse large B-Cell lymphoma and multiple myeloma: a functional assessment based on actin three-dimensional structures. Int J Mol Sci. 2020;21(9):3093. doi: 10.3390/ijms21093093.
28. Chen J, Zhao D, Zhang L, Zhang J, Xiao Y, Wu Q, et al. Tumor-associated macrophage (TAM)-derived CCL22 induces FAK addiction in esophageal squamous cell carcinoma (ESCC). Cell Mol Immunol. 2022;19(9):1054–1066. doi: 10.1038/s41423-022-00903-z.
29. Li X, Tian W, Jiang Z, Song Y, Leng X, Yu J. Targeting CD24/Siglec-10 signal pathway for cancer immunotherapy: recent advances and future directions. Cancer Immunol Immunother. 2024;73(2):31. doi: 10.1007/s00262-023-03606-0.
30. Song G, Ni H, Zou L, Wang S, Tian F, Liu H, Cho W. Expression of CD40 is a positive prognostic factor of diffuse large B-cell lymphoma treated with R-CHOP (Rituximab, cyclophosphamide, doxorubicin, vincristine, and prednisone). Onco Targets Ther. 2016;9:3799–3805. doi: 10.2147/OTT.S96992.
31. Morgan D, Tergaonkar V. Unraveling B cell trajectories at single cell resolution. Trends Immunol. 2022;43(3):210–229. doi: 10.1016/j.it.2022.01.003.
32. Rui L, Drennan AC, Ceribelli M, Zhu F, Wright GW, Huang DW, Xiao Y, Li KM, Grindle L, Lu DJ, et al. Epigenetic gene regulation by janus kinase 1 in diffuse large B-cell lymphoma. Proc Natl Acad Sci USA. 2016;113(46):E7260–E7267. doi: 10.1073/pnas.1610970113.
33. Lam LT, Wright G, Davis RE, Lenz G, Farinha P, Dang L, Chan JW, Rosenwald A, Gascoyne RD, Staudt LM. Cooperative signaling through the signal transducer and activator of transcription 3 and nuclear factor-κB pathways in subtypes of diffuse large B-cell lymphoma. Blood. 2008;111(7):3701–3713. doi: 10.1182/blood-2007-09-111948.
34. Izgutdina A, Temple WC, Nix MA, Geng H, Ramos E, Naik A, Larson R, Salangsang F, Phojanakong P, Camara Serrano JA, et al. Affinity matured CD72 CAR-T improves efficacy versus low antigen density B-Cell non-hodgkin lymphoma models. Blood. 2023;142(Supplement 1):2068–2068. doi: 10.1182/blood-2023-182873.
35. Dai Y, Kizhakeyil A, Chihara D, Li X, Liu Y, Sainz Zuniga TP, Wilson A, Henderson J, Vibe D, Petrosyants A, et al. Multi-modal spatial characterization of tumor immune microenvironments identifies targetable inflammatory niches in diffuse large B cell lymphoma. Nat Genet. 2025;57(11):2715–2727. doi: 10.1038/s41588-025-02353-5.
36. Dai L, Fan G, Xie T, Li L, Tang L, Chen H, Shi Y, Han X. Single-cell and spatial transcriptomics reveal a high glycolysis B cell and tumor-associated macrophages cluster correlated with poor prognosis and exhausted immune microenvironment in diffuse large B-cell lymphoma. Biomark Res. 2024;12(1):58. doi: 10.1186/s40364-024-00605-w.
37. Noël F, Massenet-Regad L, Carmi-Levy I, Cappuccio A, Grandclaudon M, Trichot C, Kieffer Y, Mechta-Grigoriou F, Soumelis V. Dissection of intercellular communication using the transcriptome-based framework ICELLNET. Nat Commun. 2021;12(1):1089. doi: 10.1038/s41467-021-21244-x.
38. Hagn M, Sontheimer K, Dahlke K, Brueggemann S, Kaltenmeier C, Beyer T, Hofmann S, Lunov O, Barth TF, Fabricius D, et al. Human B cells differentiate into granzyme B-secreting cytotoxic B lymphocytes upon incomplete T-cell help. Immunol Cell Biol. 2012;90(4):457–467. doi: 10.1038/icb.2011.64.

39. Craig JW, Mina MJ, Crombie JL, Lacasce AS, Weinstock DM, Pinkus GS, et al. Assessment of CD52 expression in "double-hit" and "double-expressor" lymphomas: implications for clinical trial eligibility. 2018. doi: 10.1371/journal.pone.0199708.
40. Guan X, Fang T, Wang Y, Liu W, Hao M, Qiu L. High level of IL-16 secreted by Non-GCB DLBCL facilitates tumor growth though the tumor-promoting and immunosuppressive tumor microenvironment. Blood. 2023;142(Supplement 1):6080–6080. doi: 10.1182/blood-2023-180840.
41. Visco C, Li Y, Xu-Monette ZY, Miranda RN, Green TM, Li Y, Tzankov A, Wen W, Liu W, Kahl BS, et al. Comprehensive gene expression profiling and immunohistochemical studies support application of immunophenotypic algorithm for molecular subtype classification in diffuse large B-cell lymphoma: a report from the international DLBCL Rituximab-CHOP consortium program study. Leuk. 2012;26(9):2103–2113. doi: 10.1038/leu.2012.83.
42. Lenz G, Wright G, Dave SS, Xiao W, Powell J, Zhao H, Xu W, Tan B, Goldschmidt N, Iqbal J, et al. Stromal gene signatures in large-B-cell lymphomas. N Engl J Med. 2008;359(22):2313–2323. doi: 10.1056/NEJMoa0802885.
43. Wu B, Zhang B, Li B, Wu H, Jiang M. Cold and hot tumors: from molecular mechanisms to targeted therapy. Signal Transduct Target Ther. 2024;9(1):1–65. doi: 10.1038/s41392-024-01979-x.
44. Imai T, Chantry D, Raport CJ, Wood CL, Nishimura M, Godiska R, Yoshie O, Gray PW. Macrophage-derived chemokine is a functional ligand for the CC chemokine receptor 4. J Biol Chem. 1998;273(3):1764–1768. doi: 10.1074/jbc.273.3.1764.
45. Zhu F, Wang KB, Rui L. STAT3 activation and oncogenesis in lymphoma. Cancers. 2019;12:19. doi: 10.3390/cancers12010019.
46. Li YL, Shi ZH, Wang X, Gu KS, Zhai ZM. Tumor-associated macrophages predict prognosis in diffuse large B-cell lymphoma and correlation with peripheral absolute monocyte count. BMC Cancer. 2019;19(1):1–10. doi: 10.1186/s12885-019-6208-x.
47. Zeng H, Wei Y, Xie M, Yang L, Huang F, Wei X, Hao X, Feng R. CD163+ tumor associated macrophages predict inferior outcome in patients with diffuse large B-Cell lymphoma treated with R-CHOP. Blood. 2015;126(23):5023–5023. doi: 10.1182/blood.V126.23.5023.5023.
48. Li W, Wang F, Guo R, Bian Z, Song Y. Targeting macrophages in hematological malignancies: recent advances and future directions. J Hematol Oncol. 2022;15(1):1–29. doi: 10.1186/s13045-022-01328-x.
49. Lindner S, Dahlke K, Sontheimer K, Hagn M, Kaltenmeier C, Barth TFE, et al. Interleukin 21-induced granzyme B-expressing B cells infiltrate tumors and regulate t cells. Cancer Res. 2013;73(8):2468–2479. doi: 10.1158/0008-5472.CAN-12-3450.
50. Arabpour M, Rasolmali R, Talei AR, Mehdipour F, Ghaderi A. Granzyme B production by activated B cells derived from breast cancer-draining lymph nodes. Mol Immunol. 2019;114:172–178. doi: 10.1016/j.molimm.2019.07.019.
51. Revel M, Sautès-Fridman C, Fridman WH, Roumenina LT. C1q+ macrophages: passengers or drivers of cancer progression. Trends in Cancer. 2022;8(7):517–526. doi: 10.1016/j.trecan.2022.02.006.
52. Yan ZX, Dong Y, Qiao N, Zhang YL, Wu W, Zhu Y, Wang L, Cheng S, Xu P, Zhou Z, et al. Cholesterol efflux from C1QB-expressing macrophages is associated with resistance to chimeric antigen receptor T cell therapy in primary refractory diffuse large B cell lymphoma. Nat Commun. 2024;15(1):1–16. doi: 10.1038/s41467-024-49495-4.